COMPRESSIBILITY EFFECTS ON THE WAKE DYNAMICS OF A CIRCULAR CYLINDER

***I. Rodríguez*[1], *B. Eiximeno*[1,2], *L. Gasparino*[2], *C. Tur-Mongè*[1], *J. Muela*[2], *O. Lehmkuhl*[2]**

[1] ***Turbulence and Aerodynamics Research Group. Universitat Politècnica de Catalunya***

[2] ***Large-scale Computational Fluid Dynamics group. Barcelona Supercomputing Center***

ivette.rodriguez@upc.edu

Abstract

Compressible large-eddy simulations of the flow past a circular cylinder at Reynolds numbers $Re = 10^4$ and Mach numbers in the range $M = 0.2-1.2$ are performed. Changes in the wake dynamics, coherent structures and flow topology brought about compressibility effects are discussed and analysed in detail.

1 Introduction

The flow over a bluff body has received much attention due to its importance in many engineering applications. In particular, significant efforts have been devoted to the flow past a circular cylinder, which in spite of its simple geometry the flow involves many phenomena depending on the Reynolds number ($Re = \rho U_{ref} D/\mu$). The incompressible flow past cylinders has been widely studied in the literature; e.g. comprehensive descriptions about the different wakes regimes can be found in Roshko (1993); Williamson (1996). However, studies considering compressibility effects are more scarce in the literature. Compressibility dominates the flow producing, a steady increase in the drag with the Mach number, with a local maximum which precedes the absolute maximum at nearly $M = 1$. At supersonic Mach numbers, a decrease in the drag coefficient up to $M = 1.6$ occurs, above which it stabilises to a value near that of low Mach numbers.

There are several experimental works documenting the variation of the drag coefficient with the Mach number (see for instance Macha (1976); Murthy and Rose (1978)). In addition to the variation in the drag forces, compressibility also produces important changes in the flow dynamics. For instance, in the transonic regime, the flow is characterised by moving shock waves which interact with the boundary layer instabilities and the vortex shedding process, shock/turbulent boundary layer interaction in the cylinder shoulders, shock/wake interaction and the appearance of local supersonic zones in the vortex formation region.

The wake dynamics and compressibility effects have been less studied. Among these, Schmidt and Shepherd (2015) explored the wake dynamics at $M = 4$ and speculated about the possibility that periodic oscillation in the wake could be attributed to acoustics perturbations. More recently, Awasthi et al. (2022) analysed the unsteady characteristics of the wake at $M = 3$ and also suggested that the shedding in the wake is due to an acoustic resonance.

From a numerical point of view, results on the compressible flow past a circular cylinder are rather scarce and most of the studies reported have been either to test the suitability of numerical methods (e.g. Mani et al. (2009); Khalighi et al. (2010)) or preliminary studies in relatively coarse grids , see Xia et al. (2016). The complex interplay between shock waves, turbulent structures, and vortex shedding in the transonic and supersonic regimes necessitates careful consideration for understanding and predicting the flow behavior around the cylinder. Thus, in the present work, compressibility effects on the flow past a cylinder at the subcritical Reynolds number $Re = 10^4$ will be studied for the range of Mach numbers $M = 0.2 - 1.2$. This encompasses both subsonic and transonic regimes. The changes in the forces, wake dynamics and topology will be discussed in detail.

2 Mathematical and numerical models

The filtered compressible Navier-Stokes equations can be written as:

$$\frac{\partial \bar{\rho}}{\partial t} + \nabla \cdot (\bar{\rho}\tilde{\mathbf{u}}) = 0 \quad (1)$$

$$\frac{\partial (\bar{\rho}\tilde{\mathbf{u}})}{\partial t} + \nabla(\bar{\rho}\tilde{\mathbf{u}} \otimes \tilde{\mathbf{u}}) + \nabla \bar{p} - \nabla \cdot \hat{\boldsymbol{\tau}} = \nabla(\boldsymbol{\tau}_{\mathrm{SGS}}) \quad (2)$$

$$\frac{\partial (\hat{E})}{\partial t} + \nabla \cdot ((\hat{E} + \bar{p})\tilde{\mathbf{u}}) - \nabla \cdot (\hat{\boldsymbol{\tau}}\tilde{\mathbf{u}}) + \nabla \cdot (\kappa \nabla \tilde{T}) = -\nabla \cdot (\kappa_{SGS} \nabla \tilde{T}) + \nabla(\boldsymbol{\tau}_{\mathrm{SGS}}\tilde{\mathbf{u}}) \quad (3)$$

where $\mathbf{u}$, p, T stand for the velocity vector, pressure and temperature fields, respectively. ρ and E represent the fluid density and the total energy. In the equations, $\bar{\cdot}$ denotes a spatial filter operation, whereas $\tilde{\cdot}$ refers to the Favre filtered variable. The $\hat{\cdot}$ symbol represents a magnitude based on a filtered variable and not a filter operation. Hence, $\hat{E}$ is the resolved total energy and not the filtered total energy. The viscous stress tensor $\hat{\tau}$ for compressible flows consider both

the strain rate component and the dilatational one and is defined as

$$\tau = \mu(\tilde{T}) \left(\nabla\tilde{\mathbf{u}} + (\nabla\tilde{\mathbf{u}})^T - \frac{2}{3}\nabla\cdot\tilde{\mathbf{u}}I \right) \quad (4)$$

Ideal mono-atomic gas with $\gamma = C_p/C_v = 1.4$ and Prandtl number $Pr = 0.71$, is considered. Dynamic viscosity dependence with temperature is computed using the Sutherland's law

$$\mu(\tilde{T}) = 1.458 \times 10^{-6} \frac{\tilde{T}^{1.5}}{\tilde{T} + 110.4} \quad (5)$$

To close the equations an appropriate formulation for the subgrid-scale (SGS) terms $\boldsymbol{\tau}_{\mathrm{SGS}}$ is required. Its deviatoric part is modelled using an eddy viscosity approach:

$$\boldsymbol{\tau}^a_{ij} = \boldsymbol{\tau}_{ij} - \frac{\delta_{ij}}{3}\boldsymbol{\tau}_{kk} = -2\mu_{\mathrm{t}}\hat{S}_{ij} \quad (6)$$

where δ_{ij} is the Kronecker delta, $\bar{S}ij$ is the filtered strain rate tensor given by $\hat{S}_{ij} = \frac{1}{2}(\nabla\tilde{u}_i + \nabla\tilde{u}_j)$ and μ_{t} is the SGS eddy viscosity. Here, the ILSA sub-grid scale (SGS) model is used (Lehmkuhl et al., 2019).

The numerical solution to the above equations is obtained using an in-house code called Sod2d (`https://gitlab.com/bsc_sod2d/sod2d_gitlab`), which is based on a low-dissipation high-order spectral element method (SEM). The SEM combines Galerkin's finite-element continuous model with a modified version of Guermond's Entropy Viscosity stabilization, specifically tailored to work with the spectral element approach. This combination ensures numerical stability and accuracy in capturing flow features. To counter the aliasing effects of the reduced order integration imposed by using SEM, the code employs an operator split to handle the convective terms. This split helps improve the accuracy of the simulation, especially in resolving fine-scale structures. Sod2d utilizes spectral type elements, which have advantages in terms of computational cost, particularly when hexahedron-shaped elements are employed. These elements contribute to the overall efficiency of the numerical computations. For the time-advancing algorithm, the code adopts a fourth-order Runge-Kutta method. This choice of time-integration scheme ensures accurate and stable time advancement of the flow field, allowing for efficient and reliable simulations. Overall, the used methodology enables Sod2d to provide accurate and efficient solutions to the compressible flow equations, being suitable for studying complex flow phenomena as the one presented in this study.

Computational domain and boundary conditions

The compressible flow past a circular cylinder at Reynolds number $Re = \rho U_{ref} D/\mu = 10^4$, defined in terms of the cylinder diameter D and the free-stream

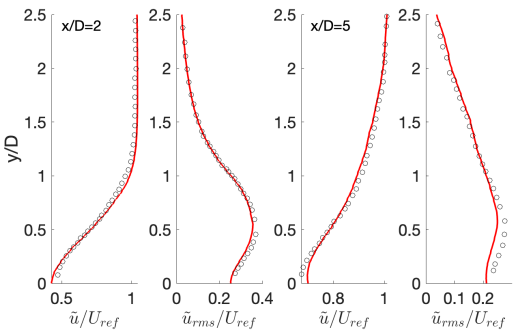

Figure 1: Streamwise velocity and its fluctuations at two streamwise locations in the wake centreline. Comparison with the LES of Khalighi et al. (2010) (dots)

U_{ref}, and Mach numbers of $M = U_{ref}/a = 0.2-1.2$, a being the sound velocity. The range of Mach numbers cover both subsonic and transonic regimes, thus it would be interesting to analyse how compressibility affects both main aerodynamic parameters and the wake topology.

Solutions are obtained in a computational domain of dimensions $x \equiv [-30D : 50D]$; $y \equiv [-30D : 30D]$; $z \equiv [0 : \pi D]$ with the cylinder located at the origin $(0,\ 0,\ 0)$. The boundary conditions at the cylinder surface are set as no-slip and adiabatic. For the far-field boundaries (outlet and inlet), a non-reflective buffer zone based on the method proposed by Wasistho et al. (1997) is applied to damp wave reflections and avoid unphysical reflections at the domain boundaries. Periodic boundary conditions are used in the spanwise direction. The computational mesh used for the simulations is semi-structured and generated by extruding a two-dimensional grid in the spanwise direction. The mesh comprises 3rd-order hexahedrons with 64 nodes per element, resulting in a total of 27.3 million nodes (approximately 414388×66 grid points). The mesh has been refined in the wake region and the vicinity of the cylinder, with special attention to the boundary layer, where a wall-resolved condition with $y^+ = u_\tau n/\nu < 1$ is implemented (where n is the normal distance from the cylinder surface, u_τ is the skin friction velocity, and ν is the kinematic viscosity). Furthermore, *a-posteriori* analysis to evaluate the ratio of the grid size (h) to the Kolmogorov scales (η) is conducted. In the cylinder wake, this ratio has been found to be $h/\eta < 12 - 14$. Since the peak in the dissipation spectrum is around $h/\eta \approx 24$ (Pope, 2001), the present grid resolution is deemed suitable for accurately resolving the flow features in the present LES.

For the computations presented here, the simulations have been advanced in time until the statistical stationary state is reached. After the initial transient is washed out, the results have been computed for a minimum of 400 time units ($t^* = tU_{ref}/D$) for cases

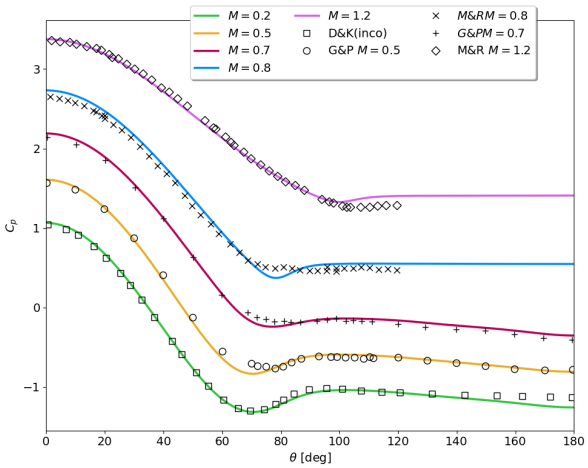

Figure 2: Pressure coefficient distribution along the cylinder circumference. Comparison with the literature. $D06$ Dong et al. (2006), $G\&P$ Gowen and Perkins (1953), $M\&R$ Murthy and Rose (1978). For clearness, results have been shifted.

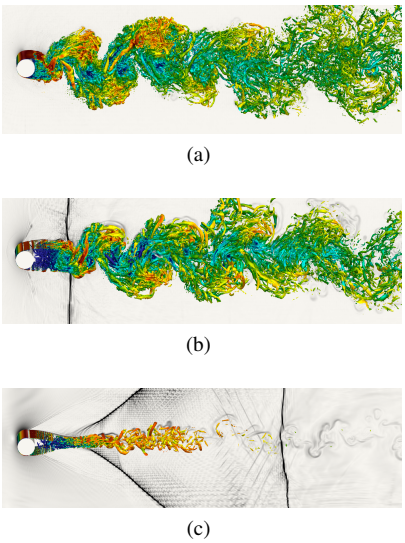

(a)

(b)

(c)

Figure 3: Instantaneous vortical structures represented by Q-isocountours $Q^* = 3$ coloured by the velocity magnitude over the density gradient field for (a) $M_0 = 0.5$, (b) $M_0 = 0.8$ and (c) $M_0 = 1.2$

where vortex shedding occurs ($M \leq 0.9$) and about 300 time units for larger Mach numbers.

To ensure the accuracy and reliability of the present setup and numerical mesh, extensive comparisons of the velocity profiles and pressure distribution have been performed. Figure 1 displays a comparison of the streamwise velocity profiles and its fluctuations with the results reported by Khalighi et al. (2010) at two downstream locations, specifically at $x/D = 2$ and $x/D = 5$. Khalighi et al. (2010) conducted compressible LES at the same Reynolds number and Mach number of 0.2 but used a coarser grid of nearly 9 million grid points ($576 \times 320 \times 48$). The figure reveals that both the first and second-order statistics exhibit a rather good agreement with the literature.

In Figure 2, the distributions of the pressure coefficient around the circumference of the cylinder are shown. The pressure coefficient is defined as $C_p = (\overline{p} - \overline{p}_{ref})/(1/2\overline{\rho}U^2_{ref})$, where $\overline{p}$ is the time-averaged pressure, and $\overline{p}_{ref}$ is the reference pressure. The figure includes experimental data from the literature, as well as incompressible direct numerical simulations (DNS) conducted by Dong et al. (2006) at $Re = 10000$. The experimental results correspond to larger Reynolds numbers, specifically Murthy and Rose (1978) at $Re = 5 \times 10^5$ and Gowen and Perkins (1953) at $M = 0.5$ and $Re = 8.5 \times 10^4$, and $M = 0.7$ and $Re = 9.4 \times 10^4$. Despite the differences in flow conditions, the agreement between the computed results and the literature data at various Mach numbers is reasonably good. In summary, the satisfactory agreement with the data from the literature confirms the reliability and suitability of the numerical mesh and setup for accurately simulating the compressible flow behavior at the given Reynolds number.

3 Results

Considering the various Mach numbers analyzed, i.e. $M = 0.2, 0.5, 0.7, 0.8, 0.9, 1, 1.2$, and taking into account the specific characteristics of the flow studied, our analysis is divided into three distinct regimes. Firstly, we have the subsonic regime for Mach numbers up to 0.5. Secondly, there is the low transonic regime covering the range of Mach numbers from 0.7 to 0.9. Lastly, we have the high transonic regime, which encompasses Mach numbers from 1 to 1.2. To illustrate the different regimes, we present in Figure 3 visual representations of vortical structures identified using Q-isocontours superimposed on the density gradient for each specific regime. Furthermore, in Figure 4, we provide energy spectra of pressure fluctuations obtained from probes strategically positioned in the shear layers and wake, enabling the capture of both Kelvin-Helmholtz instabilities and vortex shedding frequency. These visual and spectral analyses provide valuable insights into the flow behavior and dynamics within each regime, shedding light on the distinctive characteristics and phenomena exhibited at different Mach numbers. For instance, it is seen that the strengthening and interaction of shock waves as Mach number increases play a critical role in shaping the flow characteristics, leading to distinctive phenomena such as the suppression of KH instabilities and the modification of the vortex dynamics.

In the subsonic regime, compressible effects are relatively weak, and the overall flow topology resembles that of incompressible flow at these Reynolds numbers (refer to Dong et al. (2006) at $Re = 10^4$ or Lehmkuhl et al. (2013) at $Re = 3900$). Specifi-

cally, the flow separates laminarly from the cylinder shoulders, and the transition to turbulence occurs in the separated shear layers (see figure Figure 3 top). The non-dimensional vortex shedding frequency, denoted by St_{vs}, is approximately 0.2 (see also Figure 4top) and remains constant up to $M = 0.9$. This observation is consistent with the findings reported by Murthy and Rose (1978), who noted that vortex shedding ceases at Mach numbers above 0.9. Furthermore, when computing the ratio of the frequency of the Kelvin-Helmholtz instabilities to that of the vortex shedding in the subsonic regime, the obtained values are in quite good agreement with the correlation proposed by Prasad and Williamson (1997), which is given by $f_{KH}/f_{vs} = 0.0235\ Re^{0.67} = 11.25$. In this study, the computed ratio yields values of 12.1 and 11.3 for $M = 0.2$ and $M = 0.5$, respectively. These close agreements between the calculated ratios and the correlation values validate the consistency of the observations in this regime (see also the discussion in the next section).

In the transonic regime, the flow displays a complex and dynamic behavior attributed to the presence of shock waves and significant compressibility effects. At a Mach number of 0.7, specific local regions of the flow around the cylinder reach supersonic speeds, leading to intermittent shock waves. This results in larger flow fluctuations compared to lower Mach numbers. The unsteady or travelling shock waves create a highly dynamic and unsteady flow environment. The travelling shocks sometimes accumulate and their movement induces pressure waves propagating and interacting with the vortex formation region. Consequently, the transition to turbulence location shifts toward the cylinder shoulder, while vortex shedding becomes more pronounced, causing shear-layers to oscillate at the vortex shedding frequency. As a consequence of this enhanced vortex shedding, the presence of Kelvin-Helmholtz (KH) instabilities becomes barely detectable in the probes located within the shear-layers (see figure Figure 4 bottom).

With a further increase in the Mach number, the intensity of shock waves becomes more pronounced, and quasi-stationary shock waves emerge both on the cylinder shoulder and normal to the developing shear layers. This is what was called by Zdravkovich (1997); **?** the permanent shock regime. The shear layers exhibit minimal oscillation at the end of the vortex formation zone, and their modulation frequency aligns with the vortex shedding frequency. Consequently, there is a noticeable enlargement of the vortex formation zone. Additionally, the frequency of Kelvin-Helmholtz (KH) instabilities decreases with the Mach number, and the ratio of their frequency to the vortex shedding frequency is measured to be 7.5 for $M = 0.8$ and 3.6 for $M = 0.9$.

These findings underscore the significant impact of shock waves on the flow behavior and the transition to turbulence within this range of Mach numbers. Such changes bring about distinctive modifications in the vortex dynamics and shear-layer characteristics.

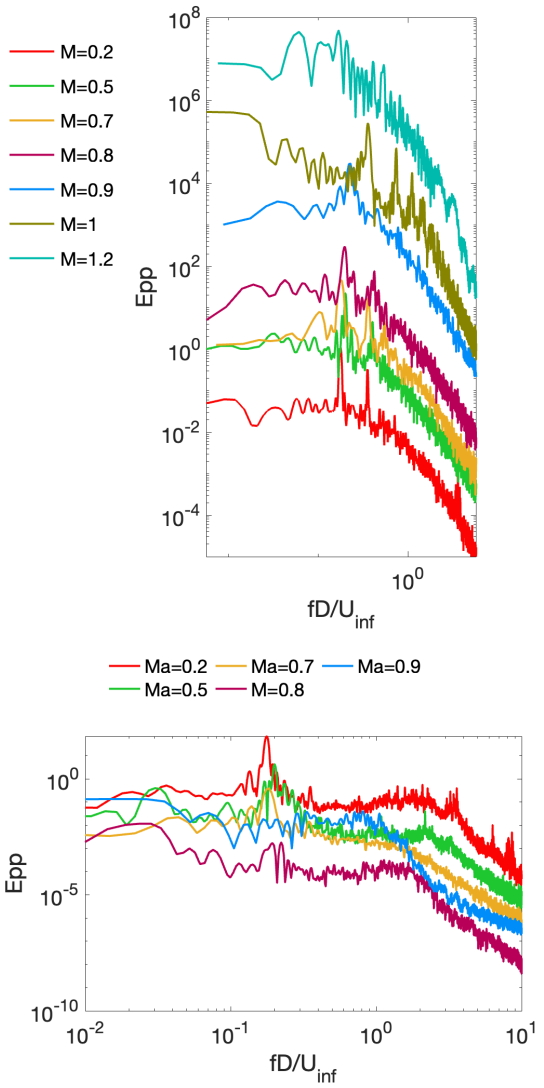

Figure 4: Energy spectra of the pressure fluctuations (top) for a probe located in the wake of the cylinder. Spectra have been shifted for clearness. (bottom) for a probe located in the separated shear-layers.

In the upper transonic regime, significant changes in the flow behavior are induced by the intensified shock waves. At a Mach number of 1, oblique shock waves form on the cylinder shoulder, dominating the separation mechanisms and delaying the detachment of the boundary layer. As a consequence, the shear layers converge towards the wake centerline. Additionally, downstream of the cylinder, a pair of λ-shock waves settles at the end of the vortex formation zone. The presence of these shock waves in this zone has the effect of suppressing Kelvin-Helmholtz (KH) high-frequency structures and eventually decoupling the vortex formation zone from the downstream wake when the Mach number exceeds 1 (as shown in

Figure 3). In fact, the observed downstream wake is uncoherent, and as previously mentioned, the vortex shedding frequency is not detected in any numerical probe located downstream of the cylinder.

Overall, important changes are brought about compressibility effects in the wake dynamics, which in turn significantly influences the aerodynamic forces acting on the cylinder as is discussed hereafter.

Mean flow characteristics

Figure 5a shows the effects of the compressibility on the drag coefficient. Moreover, results from the available literature are also depicted. It is worth noting that with the exception of the incompressible DNS by Dong et al. (2006) and the compressible LES by Khalighi et al. (2010), which are at the same Reynolds number, experimental results are reported at considerably larger Reynolds numbers. In general, a rather good agreement with the reference data is observed, especially for $M \leq 0.8$.

In Figure 5a, the effects of compressibility on the drag coefficient are illustrated, along with results from the available literature. Notably, except for the incompressible Direct Numerical Simulation (DNS) study by Dong et al. (2006) and the compressible Large Eddy Simulation (LES) conducted by Khalighi et al. (2010), which share the same Reynolds number, experimental results are reported at significantly higher Reynolds numbers. Overall, there is a reasonably good agreement with the reference data, particularly for Mach numbers up to 0.8. The trends and values of the drag coefficient align well with the reported results, validating the reliability and accuracy of the present analysis, especially in the subsonic and low transonic regimes (Mach numbers less than or equal to 0.8). Larger deviations in the drag coefficient are observed for Mach numbers above 0.8. The reasons for these deviations are not entirely clear, and they could be attributed to various factors. One possible factor is the increasing influence of Reynolds number effects at higher Mach numbers. Additionally, differences in experimental conditions, interference effects, or other experimental uncertainties might contribute to these discrepancies. Despite these variations, the numerical results still demonstrate a similar trend to the behavior observed in the experiments.

Specifically, in the subsonic regime up to approximately $M = 0.7 - 0.75$, there is an increase in the drag coefficient. This increase is primarily a result of the combined effects of an increase in stagnation pressure and a more negative base pressure coefficient, as shown in Figure 2. The decrease in the base pressure coefficient at these Mach numbers can be attributed to the transition to turbulence occurring closer to the cylinder shoulder, leading to increased turbulence production in this region.

Beyond $M = 0.7 - 0.75$, there is a subsequent decrease in the drag coefficient, reaching a local minimum value of $C_D = 1.351$ in this study, at $M = 0.9$. This decrease in drag is accompanied by a steady increase in the base pressure coefficient and a shift in the location of the local minimum pressure coefficient toward the cylinder shoulder, while its absolute value increases (as observed in Figure 2). Notably, these changes in the drag coefficient coincide with the flow entering the so-called permanent shock wave regime. Actually as it was commented before, at $M = 0.7$ intermittent shock waves occurring in the cylinder shoulder and along the shear layers and associated pressure fluctuations energises the shear layer causing the increase in the fluctuations and in the drag coefficient. At higher Mach numbers, the variations in the drag coefficient is a consequence of the interplay between shocks and expansions which causes the further reduction of the pressure coefficient minimum value, the displacement of the flow separation towards the cylinder rear end and the increase in the base pressure coefficient. All these changes brought about the increased compressibility affects the wake topology as previously discussed in the instantaneous flow and can be seen in Figure 6, where the topology of the near wake for $M = 0.8$ and $M = 1.2$ is depicted.

4 Conclusions

In this study, compressible large-eddy simulations were conducted to investigate the flow past a cylinder at a Reynolds number of 10^4 across the subsonic and transonic regimes up to a Mach number of $M = 1.2$. The variation of drag over this Mach number range exhibited consistent values and trends with those reported in existing literature.

Compressibility was found to significantly impact the transition to turbulence location and mechanism. As the Mach number increased and approached the drag maximum value at around $M = 0.7$, the transition to turbulence shifted towards the cylinder shoulder. Once the flow entered the so-called permanent shock regime at approximately $M = 0.8$, the presence of steady normal shocks resulted in the enlargement of the vortex formation region, thereby delaying the transition to turbulence. Further increases in the Mach number led to the delay of flow separation from the cylinder, causing the shear layers to converge towards the cylinder wake centerline. In these high Mach number conditions, the wake coherence was lost, and the vortex shedding frequency could not be detected in any numerical probe along the wake. Overall, the simulations provided valuable insights into the complex flow behavior and the impact of compressibility on the flow dynamics.

Acknowledgments

This work has been partially financially supported by the Ministerio de Economía y Competitividad, Secretaría de Estado de Investigación, Desarrollo e Innovación, Spain (ref. PID2020-116937RB-C21 and PID2020-116937RB-C22). O.L. has been partially

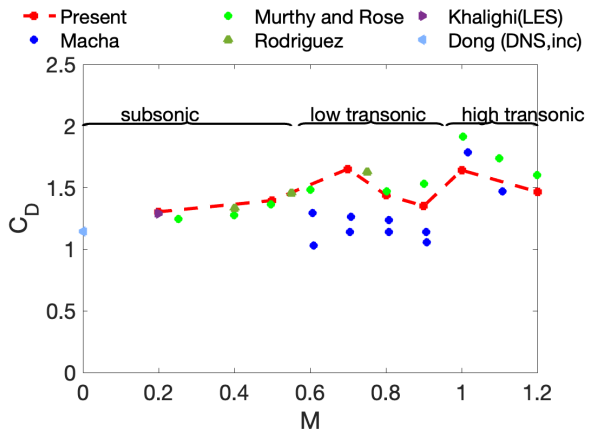

Figure 5: (a) Variation of the drag coefficient with the Mach number. Comparison with the literature. Macha (1976) $Re = 10^5 - 10^6$,Rodriguez (1984) $Re = 10^5$, Murthy and Rose (1978) $Re = 8.3 \times 10^4$, Khalighi et al. (2010); Dong et al. (2006) $Re = 10^4$.

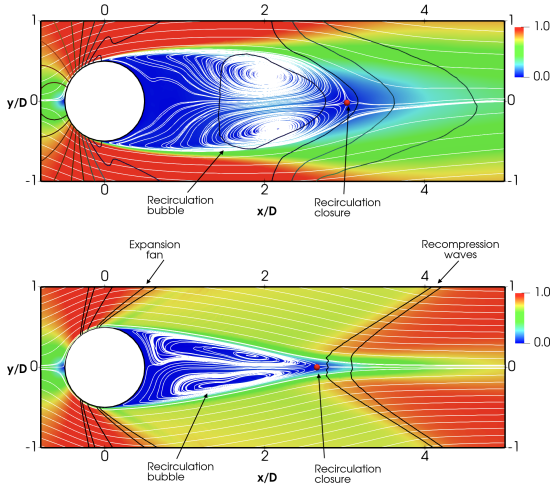

Figure 6: Time-average near wake velocity field. (top) $M_0 = 0.8$, (bottom) $M_0 = 1.2$

supported by a Ramon y Cajal postdoctoral contract (Ref: RYC2018-025949-I). I.R. also acknowledges fundings by AGAUR (Ref. 2021 SGR 01051).

References

Awasthi, M., McCreton, S., Moreau, D. and Doolan, C. (2022), 'Supersonic cylinder wake dynamics', *Journal of Fluid Mechanics* **945**, A4.

Dong, S., Karniadakis, G. E., Ekmekci, A. and Rockwell, D. (2006), 'A combined direct numerical simulation-particle image velocimetry study of the turbulent near wake', *Journal of Fluid Mechanics* **569**, 185.

Gowen, F. and Perkins, E. (1953), Drag of circular cylinders for a wide range of Reynolds numbers and Mach numbers, Technical Report NACA TN 2960, Ames Aeronautical Laboratory.

Khalighi, Y., Mani, A., Ham, F. and Moin, P. (2010), 'Prediction of sound generated by complex flows at low mach numbers', *AIAA Journal* **48**(2), 306–316.

Lehmkuhl, O., Piomelli, U. and Houzeaux, G. (2019), 'On the extension of the integral length-scale approximation model to complex geometries', *International Journal of Heat and Fluid Flow* **78**.

Lehmkuhl, O., Rodríguez, I., Borrell, R. and Oliva, A. (2013), 'Low-frequency unsteadiness in the vortex formation region of a circular cylinder', *Physics of Fluids* **25**(8), 085109.
URL: *http://aip.scitation.org/doi/10.1063/1.4818641*

Macha, J. M. (1976), A wind tunnel investigation of circular and straked cylinders in transonic cross flow, Technical Report NASA-CR-149372, NASA.

Mani, A., Larsson, J. and Moin, P. (2009), 'Suitability of artificial bulk viscosity for large-eddy simulation of turbulent flows with shocks', *Journal of Computational Physics* **228**(19), 7368–7374.

Murthy, V. S. and Rose, W. C. (1978), 'Detailed Measurements on a Circular Cylinder in Cross Flow', *AIAA Journal* **16**(6), 549–550.

Pope, S. B. (2001), *Turbulent Flows*, Cambridge University Press.

Prasad, A. and Williamson, C. (1997), 'The Instability of the Shear Layer Separating From a bluf body', *J. Fluid Mech.* **333**, 375–402.

Rodriguez, O. (1984), 'The circular cylinder in subsonic and transonic flow', *AIAA Journal* **22**(12), 1713–1718.

Roshko, A. (1993), 'Perspectives on Bluff Body Wakes', *Journal of Wind Engineering and Industrial Aerodynamics* **49**, 79–100.

Schmidt, B. E. and Shepherd, J. E. (2015), 'Oscillations in cylinder wakes at Mach 4', *Journal of Fluid Mechanics* **785**, R3.

Wasistho, B., Geurts, B. J. and Kuerten, J. G. (1997), 'Simulation techniques for spatially evolving instabilities in compressible flow over a flat plate', *Computers and Fluids* **26**(7), 713–739.

Williamson, C. H. K. (1996), 'Vortex dynamics in the cylinder wake', *Annual Review of Fluid Mechanics* **28**(1), 477–539.

Xia, Z., Zuoli, X., Yipeng, S. and Shiyi, C. (2016), 'Mach number effect of compressible flow around a circular cylinder', *AIAA Journal* **54**(6), 2004–2009.

Zdravkovich, M. (1997), *Flow Around Circular Cylinders: Volume I: Fundamentals*, Oxford University Press.